Advances in Applied Energy 17 (2025) 100206

Contents lists available at ScienceDirect

Advances in Applied Energy

journal homepage: www.elsevier.com/locate/adapen

Boosting direct-ethane solid oxide fuel cell efficiency with anchored palladium nanoparticles on perovskite-based anode

Shuo Zhai [a,*], Junyu Cai [a], Idris Temitope Bello [b,c,d,**], Xi Chen [b], Na Yu [b], Rubao Zhao [a], Xingke Cai [e], Yunhong Jiang [a], Meng Ni [b,*], Heping Xie [a,*]

[a] State Key Laboratory of Intelligent Construction and Healthy Operation and Maintenance of Deep Underground Engineering, Shenzhen University & Sichuan University, Shenzhen 518060, China
[b] Department of Building and Real Estate, Research Institute for Sustainable Urban Development (RISUD) & Research Institute for Smart Energy (RISE), The Hong Kong Polytechnic University, Hung Hom, Kowloon, Hong Kong, China
[c] Centre for Advances in Reliability and Safety (CAiRS), Hong Kong SAR, China
[d] School of Aerospace and Mechanical Engineering, University of Oklahoma, Norman, Oklahoma, USA
[e] Institute for Advanced Study, Shenzhen University, Shenzhen 518060, China

ARTICLE INFO

Keywords:
Solid oxide fuel cell
Anode
Ethane fuel
Pd nanoparticles
Adsorption energy

ABSTRACT

An efficient anode catalyst for hydrocarbon fuel in Solid Oxide Fuel Cells (SOFC) should possess a stable phase structure, high catalytic efficiency, and excellent coke resistance. However, traditional nickel-based anodes necessitate high steam-to-carbon ratios to prevent coking, complicating system design and reducing the overall performance. In this work, we report a nickel-free $PrBaFe_{1.9}Pd_{0.1}O_{5+\delta}$ perovskite as anode material for direct ethane SOFC, which demonstrates superior electroactivity and chemical stability. Under a reducing atmosphere, Pd nano-catalysts exsolved in-situ are uniformly anchored to the perovskite surface. Density functional theory analyses reveal that the Pd exsolution significantly improve ethane adsorption capacity, thereby reducing activation resistance and boosting catalytic performance. When used as an anode for an SDC electrolyte-supported SOFC, superior performance is achieved with the peak power densities (PPDs) of 702 and 377 mW cm^{-2} at 800 °C when using hydrogen and almost dry ethane (3% H_2O) as fuel, respectively. Moreover, the cell exhibits a stable continuous operation over 90 h under almost dry ethane atmosphere at 178 mA cm^{-2}, presenting a promising pathway for developing high-performance, nickel-free SOFC anodes that simplify system design and improves efficiency when operating with hydrocarbon fuels, thus holding significant potential for practical SOFC applications.

1. Introduction

To reduce modern society dependence on fossil fuels and achieve the triple goals of Ecology, Economy, and Efficiency, embracing renewable energy sources and energy storage technologies is crucial [1]. Solid oxide fuel cells (SOFCs) have emerged as a highly promising technology for low-emission power generation [2,3]. Unlike polymer exchange membrane fuel cells (PEMFCs), which require hydrogen as a fuel and thus face significant challenges related to storage and handling, SOFCs can operate directly on a variety of hydrocarbons (HCs) such as methane, ethane, and n-butane [4]. This flexibility eliminates the need for external reformers, which are necessary for PEMFCs but compromise their overall system complexity [5].

However, the widespread adoption of SOFCs is hindered by several challenges. Operating SOFCs with HC fuels typically requires high steam-to-carbon (S/C) ratios (>2) to prevent carbon deposition on the anodes, which leads to significant system enlargement and complexity due to the need for large amounts of water and precise control systems [6]. Reducing or eliminating the need for humidified conditions would greatly simplify SOFC systems. Yet, operating SOFCs at low S/C ratios generally results in performance degradation due to severe coking, especially with traditional nickel-based cermet anodes, which are highly

* Corresponding authors.
** Corresponding author at: Department of Building and Real Estate, Research Institute for Sustainable Urban Development (RISUD) & Research Institute for Smart Energy (RISE), The Hong Kong Polytechnic University, Hung Hom, Kowloon, Hong Kong, China.
E-mail addresses: shuo.zhai@szu.edu.cn (S. Zhai), idris-temitope.bello@connect.polyu.hk (I.T. Bello), meng.ni@polyu.edu.hk (M. Ni), xiehp@scu.edu.cn (H. Xie).

https://doi.org/10.1016/j.adapen.2025.100206
Received 19 November 2024; Received in revised form 3 January 2025; Accepted 4 January 2025
Available online 5 January 2025

prone to hydrocarbon cracking [7].

To address these challenges, alternative anode materials are being extensively investigated [8]. Perovskite oxides (ABO_3) and their derivatives, such as double perovskites ($A_2BB'O_{5+\delta}$ or $AA'B_2O_{5+\delta}$) and Ruddlesden-Popper phases ($A_{n+1}B_nO_{3n+1}$), have shown significant promise due to their structural flexibility and the ability to tailor their physical and chemical properties for enhanced electrochemical and catalytic performance [9]. Notable examples include $La_{0.75}Sr_{0.25}Cr_{0.5}Mn_{0.5}O_{3-\delta}$ [10], $La_{0.6}Sr_{0.4}FeO_{3-\delta}$ [11], and $SrFe_{0.75}Mn_{0.25}O_{3-\delta}$ [12]. These materials demonstrate sufficient catalytic activity and stability under different conditions, making them suitable candidates for SOFC anodes. Among the perovskite family, $PrBaFe_2O_{5+\delta}$ (PBF) stands out and exhibits extremely remarkable advantages under high-temperature reducing atmospheres. Studies have demonstrated that in high-temperature reducing environments, PBF can maintain its structural integrity and chemical stability, which shows obvious superiority compared to many other perovskite materials. In terms of electrochemical performance, it can efficiently facilitate electron transfer and ion migration during electrode reactions [13]. The enhanced oxygen ion diffusivity and the presence of surface defect sites endow it with excellent activity and catalytic efficiency [14]. However, despite these advantages, the electrical conductivity of PBF decreases under reducing conditions, and its electrocatalytic reactivity for hydrogen oxidation remains suboptimal [15].

Recent studies have shown that doping perovskite oxides with transition metals can significantly enhance their electrocatalytic properties [16]. In particular, the introduction of small amounts of noble metals such as palladium (Pd) into the B-site of perovskite structures has drawn significant attention. Pd is capable of serving as a catalytically active site for fuel oxidation. Moreover, the doping of Pd leads to a lower polarization resistance of the electrode, thereby improving the oxidation performance of hydrogen and hydrocarbon fuels [17]. However, there is still a lack of comprehensive research to elucidate the mechanisms of catalytic enhancement associated with noble metal doping, which is essential for designing efficient metal-oxide interfaces in SOFCs.

In this work, we develop anode materials based on the unique composition, $PrBaFe_{2-x}Pd_xO_{5+\delta}$ ($PBFPd_x$, x = 0, 0.1, 0.2), to exploit the absence of Ni in these materials and leverage the potential of PBF and Pd doping to enhance oxidation properties for hydrogen and ethane fuels in SOFC. Through extensive physicochemical and electrochemical evaluations, the influence of Pd doping on both the structural stability and catalytic activity of the catalyst was elucidated. In a reducing atmosphere, the optimized $PrBaFe_{1.9}Pd_{0.1}O_{5+\delta}$ ($PBFPd_{0.1}$) anode, featuring a cubic symmetric perovskite main phase and in-situ exsolved Pd nanocatalysts, exhibits high electrocatalytic activity and outstanding durability under hydrocarbon operation conditions. For instance, the single cell with the configuration of $PBFPd_{0.1}$-SDC|SDC|BSCF-SDC, demonstrates promising PPDs of 702 and 377 mW cm^{-2} at 800 °C when using H_2 and C_2H_6 as fuel, respectively. Moreover, the single cell maintains stable operation for over 90 h using nearly dry ethane (containing only 3% H_2O). This work represents a significant step forward developing high-performance, nickel-free SOFC anodes capable of operating efficiently with HC fuels under low-humidified conditions, simplifying SOFC systems and enhancing their viability for practical applications.

2. Experimental

2.1. Anode preparation

$PBFPd_x$ (with x = 0, 0.1, 0.2) and $Ba_{0.5}Sr_{0.5}Co_{0.8}Fe_{0.2}O_{3-\delta}$ powders were produced using the EDTA-citric acid combustion technique which is scalable and allows for the precise production of high-purity oxides, making it ideal for industrial SOFC anode manufacturing. Initially, in the experiment, $Pr(NO_3)_3{\cdot}6H_2O$, $Ba(NO_3)_2$, $Fe(NO_3)_3{\cdot}9H_2O$ and Pd ($OCOCH_3$) were used. The corresponding weights were measured according to the proportion and dissolved in pure water to prepare the solution for the following steps. Subsequently, EDTA and citric acid were added to the solution, and the pH level was adjusted with ammonia. The resulting solution was continuously stirred until it developed a gel-like substance. This gel was dried at 200 °C in an oven for 6 h, creating a black precursor. To produce the PBFPdx powders, the precursor was subjected to calcination at 1100 °C in an air atmosphere for 5 h. Finally, these powders underwent reduction by being treated in hydrogen at 800 °C for 2 h.

2.2. Characterization

The crystallinity and structure of the samples were analyzed using X-ray diffraction (XRD) with a Rigaku Ultima IV system. Rietveld refinement was performed using FullProf software for detailed lattice parameter evaluation. For Hydrogen Temperature-programmed Reduction (H_2-TPR), using approximately 60 mg of powder, the sample was exposed to a hydrogen atmosphere at 300 °C with a flow rate of 50 mL/min for an hour. Following cooling to ambient temperature, the environment was altered to 10 vol.% H_2-Ar, and then gradually heated to 800 °C at a rate of 10 °C/min. Morphological examination was conducted using scanning electron microscopy (SEM) with a TESCAN MIRA LMS, and transmission electron microscopy (TEM) with a FEI Tecnai G2 F20, coupled with energy-dispersive X-ray spectroscopy (EDX) for elemental distribution analysis. The Brunauer-Emmett-Teller (BET) test on the Micromeritics ASAP2460 instrument is carried out by first degassing about 60 mg of powder sample at 200 °C for 7 h, then cooling to liquid nitrogen temperature and introducing nitrogen to achieve adsorption equilibrium at a certain flow rate. The adsorption data at different relative pressure are recorded to form an adsorption isotherm, and finally the BET equation is fitted through software to calculate the specific surface area. The X-ray photoelectron spectroscopy (XPS) on a Thermo Scientific K-Alpha system was used to determine the valence states of surface elements, which were subsequently analyzed with Avantage software. At the Pohang Synchrotron Radiation Facility's BL7D station in South Korea, X-ray absorption spectroscopy (XAS) measurements were carried out. Following this, the acquired XAS data underwent processing using ATHENA software, which is part of the IFEFFIT suite (version 1.2.12). The oxygen vacancy concentration was measured using a Bruker A300 Electron Paramagnetic Resonance (EPR) spectrometer under low - temperature conditions. First, the sample was placed in a special sample tube and then positioned in the instrument's sample chamber. Parameters such as magnetic field strength, sweep width, and frequency were set. The sample was irradiated with a microwave source while maintaining the low - temperature environment. The signal intensity was recorded through multiple scans. When testing the carbon peaks of a material by Raman spectroscopy, fix the sample on the stage, excite it with a 532 nm laser, scan and record the spectrum, and then analyze the positions and intensities of the carbon peaks. For the purpose of conductivity testing, an exact mass of 0.6 g of the PBFPdx powder was weighed and subsequently introduced into a custom-engineered die. Uniaxial pressing was then executed under a precisely regulated pressure of 7MPa to guarantee uniform compaction. Subsequently, the pressed bars were transferred to a high-temperature sintering furnace and underwent sintering at 1100 °C for a period of 10 h, with a heating rate set at 5 °C per minute. Silver wires and silver paste were used to connect the testing terminals at equal intervals. Thereafter, conductivity measurements were carried out using a Keithley 2400 source meter via a four-probe DC method.

2.3. Cell fabrication

Single cells were fabricated with the configuration $PBFPd_x$-SDC cathodes, SDC electrolytes, and BSCF-SDC anodes. SDC electrolyte pellets with high density were prepared by pressing 0.2 g of SDC powder (sourced from Fuel Cell in the USA) and sintering at a temperature of 1300 °C for a duration of 10 h. A cathode slurry comprising BSCF and

SDC powders in a 7:3 ratio was prepared in isopropyl alcohol. Anode slurry was similarly prepared by mixing $PBFPd_x$ and SDC powders in the same ratio. The slurries were sprayed onto the surfaces of the SDC pellet to form a triple-layer structure, followed by heating to 900 °C for a duration of 2 h to ensure adequate adhesion. The silver paste was applied in a net-like pattern to the electrodes for optimal electron capture. The assembled cells were attached to quartz tubes by applying silver paste, leaving the anode exposed for testing.

2.4. Electrochemical test

The electrochemical capability exhibited by single cells was evaluated using a Solartron1287 Electrochemical Workstation. Electrochemical Impedance Spectroscopy (EIS) spectra were recorded with a voltage amplitude of 30 mV over a frequency range from 0.1 Hz to 100 kHz under open-circuit voltage conditions. Current-power density (I-P) and current-voltage (I-V) curves were obtained using a four-point probe technique with a Keithley 2420 source meter. The anode chamber received either H_2 or humidified C_2H_6 throughout the experiment, while ambient air served as the cathode atmosphere. Both H_2 and C_2H_6 fuels were supplied at a flow rate of 80 mL min-1 (STP), to ensure optimal conditions for the evaluation.

2.5. Computational details

First-principles calculations were performed using density functional theory (DFT) within the Vienna ab initio simulation package (VASP) [18,19]. The projector-augmented wave (PAW) method [20] was employed to describe core-valence electron interactions. Exchange and correlation effects were treated within the Perdew Burke Ernzerhof (PBE) generalized gradient approximation (GGA) [21]. A kinetic energy cutoff of 500 eV was applied for the plane wave expansion. The Brillouin zone integration was performed using the MonkhorstPack [22] k-point sampling method with a K-spacing value of 0.03 2π/Å. During structure relaxation, convergence criteria for the total energy and forces were set to 1.0×10^{-5} eV and 0.002 eV/Å, respectively. Charge density difference plots were generated using vaspkit [23].

3. Results and discussion

Fig. 1a presents the XRD profiles of $PBFPd_x$ (with x = 0, 0.1, 0.2), where all the three examined samples exhibit a single-phase cubic symmetric perovskite (Space group: Pm-3m), indicating the successful incorporation of Pd into the PBF lattice. With the increase of the Pd content, the main peak of the perovskite phase shifts towards a lower degree, which implies lattice expansion due to the larger ionic radius of Pd compared to Fe (0.86 Å of Pd^{2+} vs. 0.645 Å of Fe $^{3+}$) [24–26] (**Fig. S1**). After reduction in a hydrogen atmosphere at 800 °C for 2 h, the reduced PBF sample remains a pure phase, however, new phases are detected in $PBFPd_{0.1}$ and $PBFPd_{0.2}$ (Fig. 1b). For $PBFPd_{0.1}$, Pd and BaO secondary phases are identified, corresponding to Pd (JCPDS# 01–072–0710) and BaO (JCPDS# 00–030–0143). In the case of $PBFPd_{0.2}$, an additional FeO phase (JCPDS# 01–089–0690) is observed due to phase decomposition. Moreover, the lattice expansion observed prior to reduction is still evident afterwards (Fig. 1c). Rietveld refinement of the reduced samples was conducted as illustrated in **Fig. S2**. The analyses results reveal that the cell volumes are 61.4837 Å^3, 62.024 Å^3, and 62.031 Å^3 for the reduced PBF, $PBFPd_{0.1}$, and $PBFPd_{0.2}$, respectively

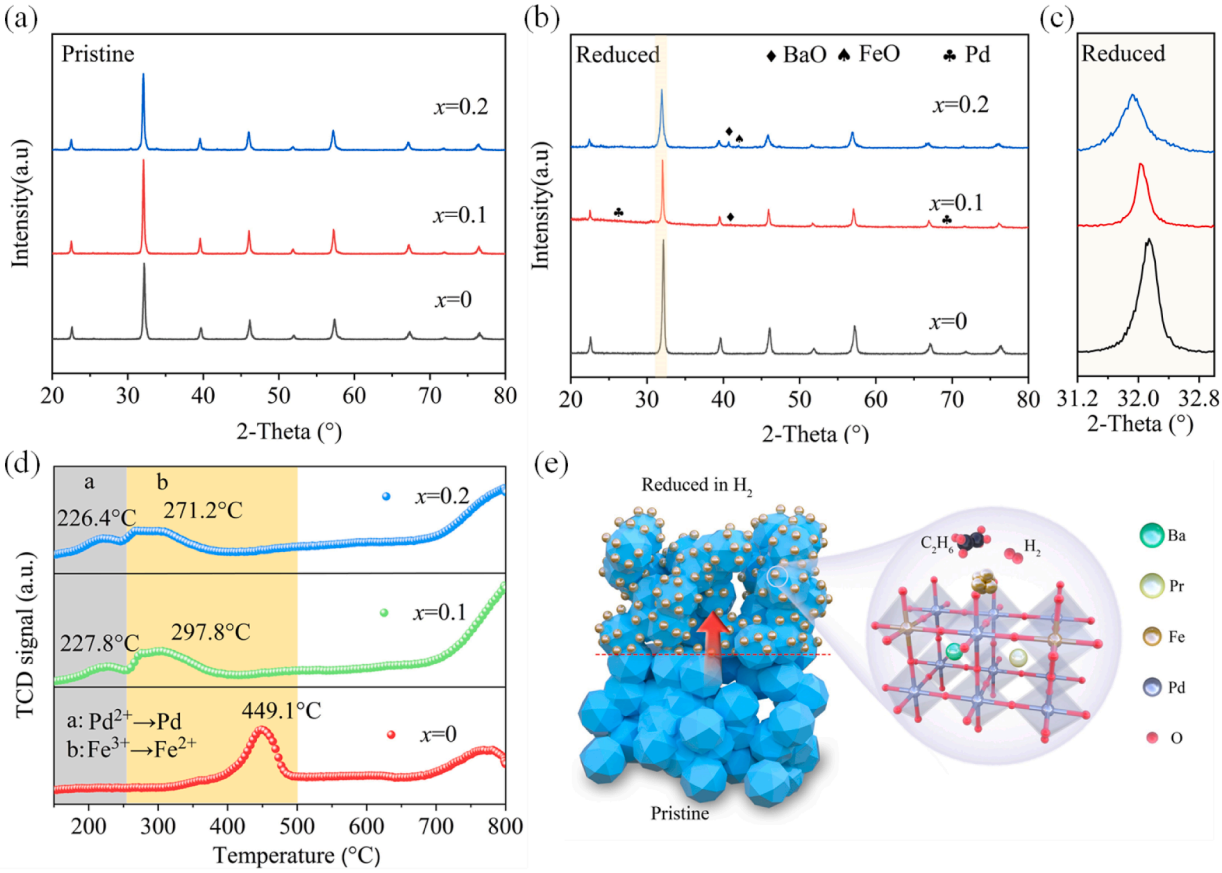

Fig. 1. XRD and H_2-TPR profiles of PBF, $PBFPd_{0.1}$, and $PBFPd_{0.2}$ (a) XRD patterns after calcination at 1100 °C in air for 5 h. (b) XRD patterns after reduction in H_2 atmosphere at 800 °C for 2 h. (c) Enlarged view of (b) between 31.5 and 33° highlighting the shift in peak positions of $PBFPd_{0.1}$ indicating lattice expansion. (d) H_2-TPR profiles of PBF, $PBFPd_{0.1}$, and $PBFPd_{0.2}$. (e) Schematic illustration of the in-situ exsolution process of Pd nanoparticles from $PBFPd_{0.1}$ under reducing a atmosphere.

(**Tables S1–S3**). Fig. 1d presents the H_2-TPR profiles of PBF, $PBFPd_{0.1}$, and $PBFPd_{0.2}$. Given the fixed valence states of Pr and Ba [27], the observed peaks were assigned to the reduction of Fe^{m+} and Pd^{m+}. The undoped PBF sample shows a broad reduction peak centered at 449.1 °C, corresponding to the reduction of Fe^{3+} to Fe^{2+} [28]. Conversely, $PBFPd_{0.1}$ and $PBFPd_{0.2}$ showcase two distinct peaks at lower temperatures (T < 400 °C). The peak at around 225 °C corresponds to the reduction of Pd species (Pd^{2+} to metallic Pd (Pd^0)), and the peak around 280 °C corresponds to the reduction of Fe reduction (Fe^{3+} to Fe^{2+}) [29], indicating that the doping of Pd lowers the reduction temperature of Fe. Notably, the H_2-TPR profiles for all samples suggest that the reduction process is incomplete at 650 °C, suggesting ongoing reduction activity even at high temperatures [17,30]. The observed low-temperature reduction in the Pd-doped samples can be attributed to the presence of Pd, which facilitates the formation of oxygen vacancies (Vö) in the lattice. These vacancies enhance the reducibility of the material by lowering the energy barrier for the reduction process. Similar studies have reported the creation of these vacancies, which can be described by the following Kröger–Vink notation:

$$PdO \rightarrow Pd'_{Fe} + V\ddot{o} + \frac{1}{2}O_2(g)$$

Fig. 1e illustrates the exsolution process occurring in $PBFPd_{0.1}$ material. Under a reducing atmosphere, Pd nano-catalysts are exsolved onto the surface of the perovskite and strongly interact with it. These exsolved catalysts serve as active sites for the adsorption and oxidation of fuels like H_2 and C_2H_6, thereby enhancing the intrinsic catalytic capabilities of the material.

To analyze the morphological evolution of $PBFPd_{0.1}$, SEM and HR-TEM were initially conducted on the sample before reduction (Fig. 2a, b). The SEM image reveals a relatively uniform particle size distribution, with particles exhibiting a smooth surface and well-defined edges (Fig. 2a). The HR-TEM image and corresponding EDX mapping reveal a well-ordered crystalline structure with uniform distribution on the perovskite pattern, indicating a high degree of crystallinity in the powder and confirming the successful incorporation of Pd before

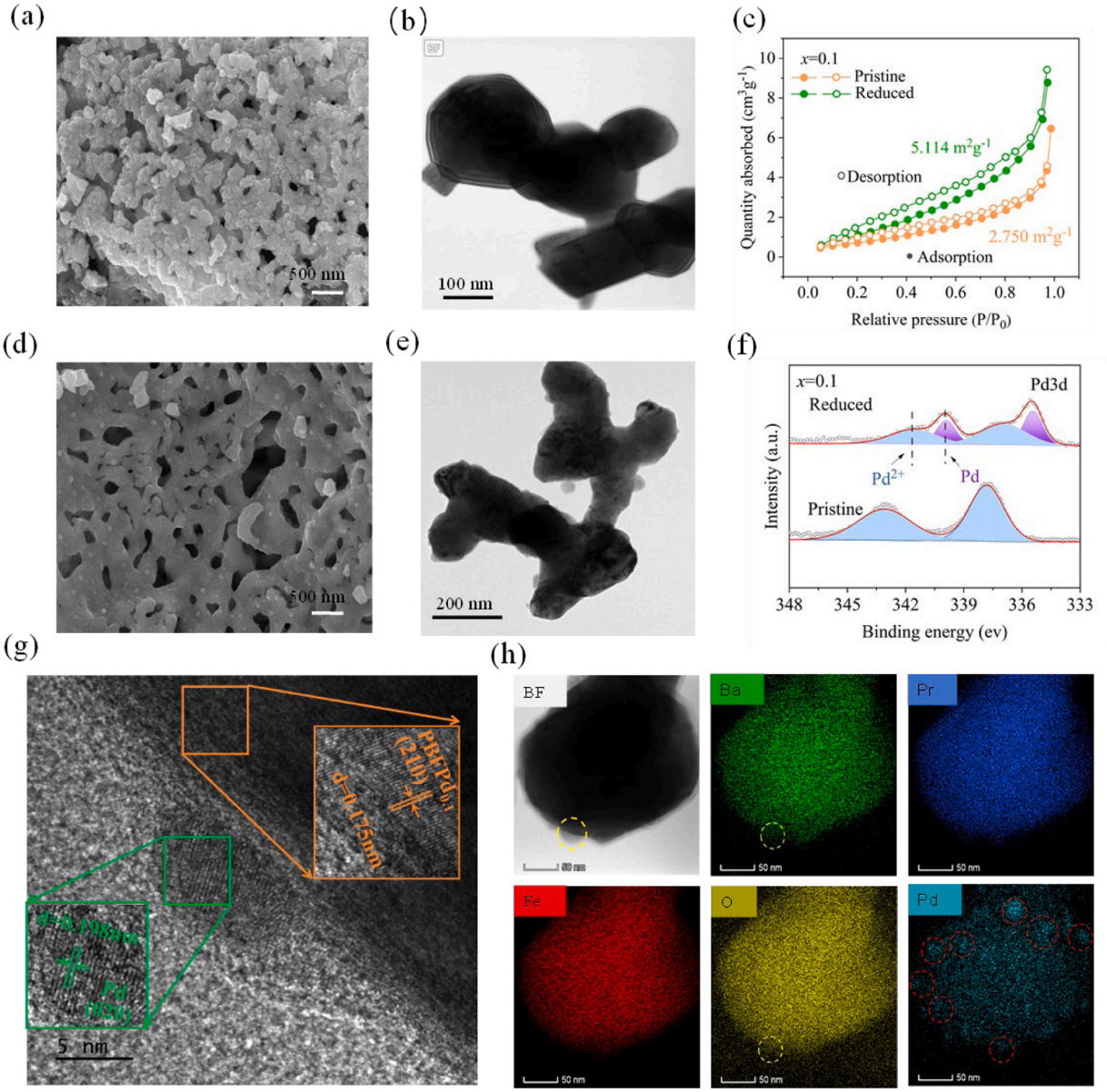

Fig. 2. (a) SEM morphology, (b) HR-TEM morphology of pristine $PBFPd_{0.1}$, (c) BET analysis of $PBFPd_{0.1}$ before and after reduction, (d) SEM morphology, (e) HR-TEM morphology of reduced $PBFPd_{0.1}$, (f) XPS Analysis of Pd Species in $PBFPd_{0.1}$ before and after reduction, (g) HR-TEM of reduced $PBFPd_{0.1}$, showing the d-spacings of the exsolved Pd nanoparticles and parent perovskite. (h) STEM image and corresponding EDX mapping of the reduced $PBFPd_{0.1}$ powder.

reduction (Fig. 2b). In contrast, the reduced PBFPd$_{0.1}$ powder displays a noticeable change in the surface morphology, with particles appearing more irregular and rougher compared to the pre-reduction state (Fig. 2d). This change in surface texture is indicative of the reduction process, exsolving the Pd metals in the form of surface defects and increased surface roughness [11,12,17]. The HR-TEM image further corroborates these observations, revealing the exsolved nanoparticles along with disordered regions and lattice distortions that were absent before reduction (Fig. 2e). Fig. 2c presents the BET analysis of the PBFPd$_{0.1}$, indicating that the specific surface area of the sample increases significantly from 2.75 m^2/g before reduction to 5.114 m^2/g after reduction. This increase in surface area can be attributed to the exsolution of nanoparticles, the formation of surface defects and the development of a more porous structure during the reduction process [27,31]. The enhanced surface area is beneficial for catalytic applications, as it provides more active sites for reactions. The XPS analysis of the pristine and reduced Pd-species in the PBFPd$_{0.1}$ and PBFPd$_{0.2}$ samples are shown in Fig. 2f and **Fig. S3**, respectively. Before reduction, Pd exists predominantly in the Pd^{2+} oxidation state, with binding energy peaks at 337.8 eV and 343.1 eV After reduction, the XPS spectrum indicates the presence of both Pd^{2+} and metallic Pd (Pd^0), with binding energy peaks at 336.8 eV / 342.4 eV for Pd^{2+} and 334.8 eV / 340.4 eV

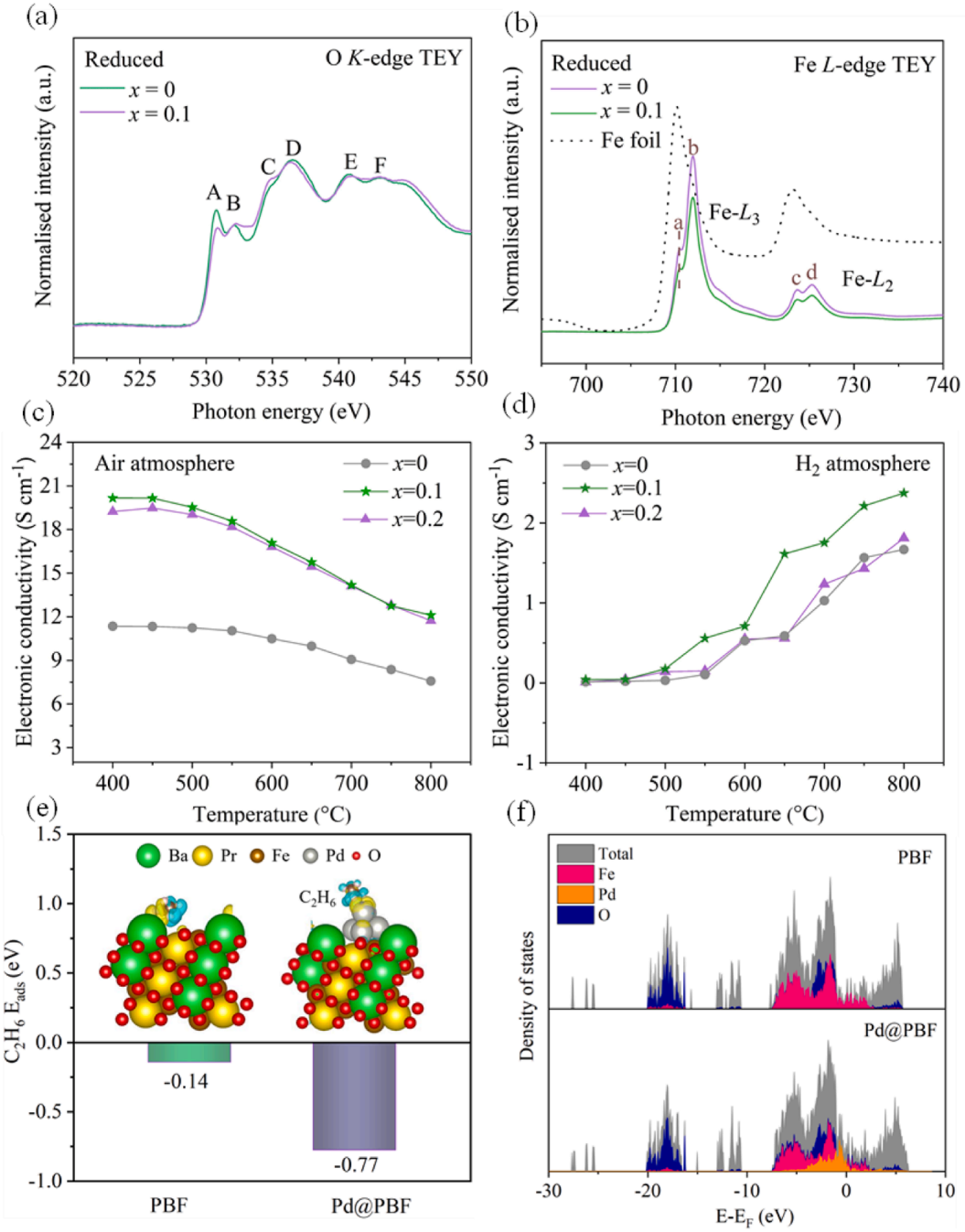

Fig. 3. XANES spectra and electronic conductivity measurements of PBFPd$_x$-SDC (x = 0, 0.1, 0.2) powders after reduction. (a) O K-edge XANES spectra in TEY mode for PBF and PBFPd$_{0.1}$. (b) Fe L-edge XANES spectra in total electron yield (TEY) mode for PBF and PBFPd$_{0.1}$ compared to Fe foil. (c) Electronic conductivity of Pd-doped PBF samples PBF, PBFPd$_{0.1}$, and PBFPd$_{0.2}$ in air atmosphere as a function of temperature. (d) Electronic conductivity of PBF, PBFPd$_{0.1}$, and PBFPd$_{0.2}$ in H_2 atmosphere as a function of temperature. (e) Charge density differences (CDD) and C_2H_6 adsorption energy (C_2H_6 E_{ads}) of the global minimum structure of ethane adsorbed on PBF (211) and Pd@PBF (211). (f) The density of states for PBF (211) and Pd@PBF (211).

for Pd^0 [12,32,33]. The coexistence of Pd^{2+} and Pd^0 suggests a partial reduction of Pd^{2+} during the reduction process, which is likely influenced by the reducing atmosphere and the interaction with the perovskite matrix (**Table S4**). Fig. 2g provides an HR-TEM image of the $PBFPd_{0.1}$ showing the d-spacings of the exsolved Pd and PBF nanoparticles. The d-spacings of the exsolved Pd and PBF are along the (102) and (210) planes, corresponding to 1.98 Å and 1.75 Å, respectively. This indicates the successful exsolution of Pd nanoparticles and their integration into the PBF matrix. Fig. 2h shows the STEM image and corresponding EDX mapping of the $PBFPd_{0.1}$ powder after reduction. The EDX mapping indicates that Pd is well-dispersed and decorated around the PBF particles due to the reduction in an H_2 environment, suggesting a homogeneous distribution of Pd with a size of around 30 nm, which is crucial for catalytic applications [17]. Therefore, the SEM and HR-TEM analyses reveal significant morphological changes in the Pd-doped PBF powder before and after reduction, highlighting the impact of the reduction process on the surface structure [32]. These findings highlight the beneficial effects of Pd doping, which not only enhances the reducibility but also modifies the electronic structure of PBF, thereby confirming its positive effect on the catalytic properties of the material.

To investigate the effect of Pd doping on the electronic structures of the samples, X-ray Absorption Near Edge Structure (XANES) measurements at the Fe-L and O-K edges were carried out on the reduced PBF and $PBFPd_{0.1}$ powders [34–36]. In total electron yield (TEY) mode, which is particularly sensitive to surface characteristics of materials, offering a probing depth of 5 nm. The O K-edge XANES spectra in TEY mode show features labeled A to F, corresponding to different oxygen environments in the lattice (Fig. 3a). The peak at 530.7 eV, designated as Peak A, can be attributed to the t_2g orbitals arising from the hybridization between the Fe3d and O 2p orbitals. Conversely, Peak B, appearing at 532.1 eV, corresponds to the e_2g orbitals involved in the Fe (Co) 3d-O 2p interaction. Compared to the reduced PBF, the reduced $PBFPd_{0.1}$ shows a lower Peak A and a wider Peak B. This pattern suggests an enhanced probability of electron transfer to the eg orbital in the reduced $PBFCN_{0.1}$, indicating a more significant reduction of Fe ions from higher to lower oxidation states [37]. Peaks C to F are associated with higher energy transitions, which are associated with Pr (Ba) 5d-O 2p orbitals and the covalent interactions between Fe/Co 4sp and O 2p orbitals. The consistent peak positions indicate that both samples have a similar oxygen environment. The Fe L-edge XANES spectra in TEY mode for the reduced PBF and $PBFPd_{0.1}$ are compared with Fe foil, as depicted in Fig. 3b. The peaks a and b correspond to the Fe-L_3 edge, while c and d correspond to the Fe-L_2 edge. The peak positions suggest that Fe is predominantly in the Fe^{3+} state in the PBF samples, with slight shifts indicating partial reduction due to Pd doping, which is consistent with the O K-edge XANES result [37,38]. Relative to TEY mode, the FY mode of soft XAS allows for offers an enhanced probing depth, reaching up to approximately 200 nm into the material [39]. Compared to the TEY, Fluorescence Yield (FY) mode provides a deeper probing capability, reaching as deep as around 200 nm within the material [40]. Similar features are observed in the FY mode, with the $PBFPd_{0.1}$ sample showing a higher intensity at the Fe-L_3 edge, indicating an increased reduction of Fe^{3+} to Fe^{2+}(**Fig. S4**).

The critical role of electrical conductivity in promoting charge transfer is fundamental to the fuel electrochemical oxidation process. Accordingly, the conductivities of the three samples are assessed using a four-point probe technique in both air and hydrogen atmospheres, across a temperature spectrum from 400 °C to 800 °C. Substitution with Pd cations markedly improves the electronic conductivity of $PBFPd_{0.1}$ and $PBFPd_{0.2}$, demonstrating conductivity levels approximately twice that of PBF when measured in an air ambiance (Fig. 3c). Additionally, enhanced conductivity can be associated with electron delocalization, which is influenced by the stronger covalent nature of the Pd-O bond compared to the Fe-O bond. This results in greater electron freedom, facilitating smoother electron movement throughout the material [41, 42]. In an H_2 atmosphere, the electronic conductivity of PBF, $PBFPd_{0.1}$, and $PBFPd_{0.2}$ samples increases with temperature (Fig. 3d). The $PBFPd_{0.1}$ sample shows significantly higher conductivity compared to the other samples. We have carried out Electron Paramagnetic Resonance (EPR) tests on three samples (**Fig. S5**). Demonstrates that the doping of Pd increases the oxygen vacancy concentration of the material. Since oxygen vacancies play a crucial role in conductivity and a higher concentration of oxygen vacancies can provide more channels for the movement of charge carriers, thus enhancing the conductivity, it indicates that Pd doping enhances the reducibility and oxygen vacancy formation the most, which in turn improves the electronic conductivity in a reducing [10,12,17]. This result confirms that $PBFPd_{0.1}$ has the optimal doping concentration of Pd compared to the other samples. The step-like conductivity profile could be attributed to the dual-pathway approach, resulting from the synergistic effects of the two distinct electron transfer modes, one is surface metal transfer and the other one is bulk phase transfer in the perovskite structure.

The initial adsorption of ethane onto the surface of the anode material is crucial for overall performance in SOFC. Given that ethane is used as fuel, the adsorption energy of ethane (C_2H_6 E_{ads}) was calculated for the molecule on PBF and Pd cluster-anchored PBF (Pd@PBF) surfaces (Fig. 3e). Pd@PBF shows a significantly higher affinity for ethane molecules compared to PBF. Specifically, the C_2H_6 E_{ads} for PBF and Pd@PBF are -0.14 eV and -0.77 eV, respectively, indicating that the Pd cluster greatly enhances the adsorption capacity of the material for ethane. The three-dimensional visualizations depict the differential charge density of the C_2H_6 molecule on the two surface models. The charge density deformation on the Pd@PBF surface is obviously stronger than that on the PBF surface, which is consistent with the calculated C_2H_6 E_{ads} results. The electronic structure evolution of PBF and Pd@PBF were analyzed from the density of states (DOS), as illustrated in Fig. 3f. The orbital contributions of Pd@PBF around the Fermi level are evidently richer than those of PBF, due to the presence of Pd. This indicates a higher concentration of charge carriers and enhanced electronic conductivity, consistent with the results of conductivity tests. Moreover, it has been revealed that the synergistic effect of Lewis acid (perovskite oxide) and Lewis base (exsolved metal) contributes to CH_4 dehydrogenation process [43]. Herein, the Lewis acid-Lewis base pairs of exsolved Pd@PBF perovskite oxide for C_2H_6 dehydrogenation process follow the same mechanism.

Having gained insights into the electronic structure and oxidation state changes in Fe induced by Pd doping in $PBFPd_x$, we then proceeded to evaluate the electrochemical performance of the SDC electrolyte-supported cells based on $PBFPd_x$-SDC (x = 0, 0.1, 0.2) anode materials, as illustrated in **Fig. S6).** Fig. 4a indicates that the undoped PBF has the lowest peak power density (PPD) of 560.8 mW/cm^2 at 800 °C compared to the $PBFPd_{0.1}$ and $PBFPd_{0.2}$. The $PBFPd_{0.1}$ sample exhibits the highest PPD of 701.6 mW/cm^2, indicating that Pd doping significantly enhances the electrochemical performance (**Fig. S7**). However, the $PBFPd_{0.2}$ shows a PPD of 594.2 mW/cm^2, which is higher than the undoped sample but lower than the $PBFPd_{0.1}$ sample, which could be attributed to the phase decomposition hindering electron transport. The superior performance of $PBFPd_{0.1}$ could be due to the exsolved Pd catalyst on the material surfaces and its high reducibility tendency in the H_2 atmosphere [17]. The ohmic impedance of the electrolyte was subtracted from the impedance spectrum to enable a better observation and comparison of the influence of Pd doping on the electrode polarization. Fig. 4b reveals a decrease in the area-specific resistance (ASR) with Pd doping, with $PBFPd_{0.1}$ showing the least ASR, about 72% and 40% times superior to PBF and $PBFPd_{0.2}$ (**Fig. S8**). This result aligns with the observed trend in the PPDs of the three samples from Fig. 4a. The DRT analysis in Fig. 4c reveals that Pd doping reduces the intensity of the polarization relaxation peaks, particularly those resulting from gas diffusion and surface and bulk diffusion processes in the P_{LF} and P_{IF} regions [44]. This is particularly significant in the $PBFPd_{0.1}$, suggesting enhanced gas diffusion as well as bulk and surface exchange processes in this material having an optimal Pd doping content of 3% [40].

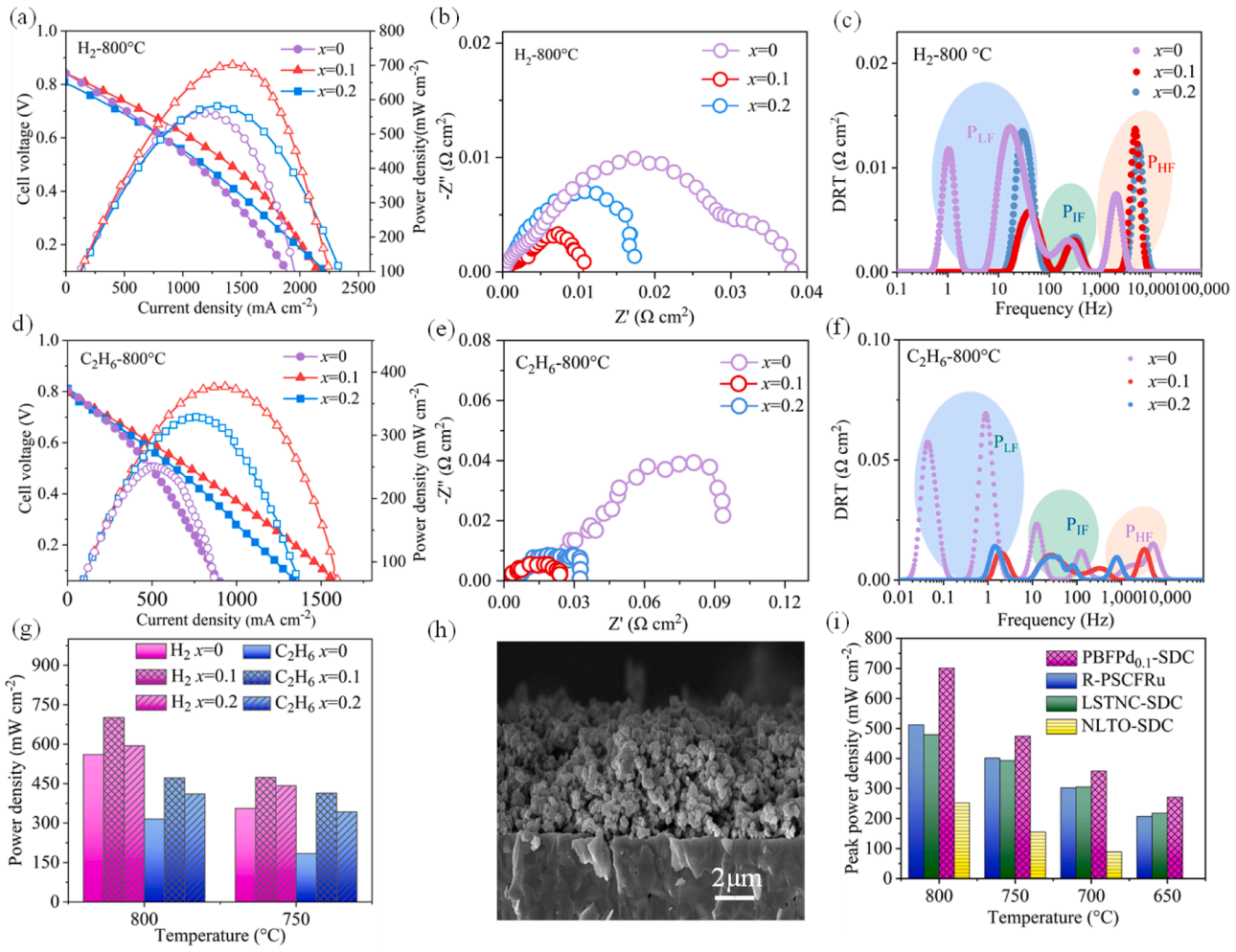

Fig. 4. Electrochemical performance and impedance spectroscopy of PBFPd$_x$-SDC| SDC | BSCF-SDC (x = 0, 0.1, 0.2) samples under different conditions. (a) I-V and power density curves for H_2 at 800 °C. (b) Nyquist plots for H_2 at 800 °C. (c) Distribution of relaxation times (DRT) for H_2 at 800 °C. (d) I-V and power density curves for C_2H_6 at 800 °C. (e) Nyquist plots for C_2H_6 at 800 °C. (f) DRT for C_2H_6 at 800 °C. (g) Power density comparison at 750 °C and 800 °C in H_2 and C_2H_6 atmospheres. (h) SEM image showing the cross-section of a cell based on the PBFPd$_x$-SDC as the anode. (i) Peak power density comparison of PBFPd$_{0.1}$ with other materials under H_2 atmosphere at various temperatures.

Fig. 4d reveals similar trends under C_2H_6 atmosphere. The undoped PBF exhibits the least PPD of 252.2 mW/cm^2, while the PBFPd$_{0.1}$ sample has the highest PPD of 377.2 mW/cm^2, and the PBFPd$_{0.2}$ with an intermediate value of 328.3 mW/cm^2 (**Fig. S9**). The impedance spectra (Fig. 4e, **Fig. S10**) show significantly higher resistance for the PBF sample, while Pd-doped samples, particularly PBFPd$_{0.1}$, show much lower resistance. The DRT profiles for C_2H_6 show similar improvements with Pd doping (Fig. 4f), where the PBFPd$_{0.1}$ sample exhibits the lowest relaxation peaks. The enhanced gas diffusion process can be attributed to the improved adsorption capacity for ethane induced by the formation of Pd clusters. The PPDs of PBFPd$_{0.1}$-based samples (Fig. 4g) remain consistently higher across both H_2 and C_2H_6 atmospheres at 800 °C and 750 °C, highlighting the beneficial effect of optimal Pd doping on performance at various temperatures. The SEM images in Fig. 4h reveal a porous, well-defined, and uniform microstructure for the PBFPd$_{0.1}$-SDC anode well fused to the electrolyte after test, which is crucial for consistent electrochemical performance. The enhanced microstructure likely contributes to the improved catalytic activity observed in the electrochemical measurements of the PBFPd$_x$-SDC (x = 0, 0.1, 0.2)-based cells [33]. Across a temperature range of 650–800 °C, the PBFPd$_{0.1}$-SDC anode cell demonstrates superior peak power density (PPD) when compared to other state-of-the-art SDC/GDC electrolyte-supported cells with recently reported anodes under H_2 atmosphere, such as $Pr_{0.6}Sr_{0.4}Co_{0.2}Fe_{0.75}Ru_{0.05}O_{3-\delta}$, $La_{0.52}Sr_{0.28}Ti_{0.94}Ni_{0.03}Co_{0.03}O_{3-\delta}$, $NaLaTiO_4$-$Sm_{0.2}Ce_{0.8}O_{2-\delta}$ [31,45] (Fig. 4i, Table S5). Such performance further underscores the effectiveness of optimal Pd doping in enhancing the electrochemical performance of PBF samples. Hence, the results in Fig. 4 strongly support the hypothesis that Pd doping significantly enhances the electrochemical performance of PBF samples.

To assess the impact of Pd doping on the cost of the anode material, we calculated the costs of four different materials. As shown in Fig. 5 and **Table S6**, the Pd-doped PBFPd$_{0.1}$ material costs approximately $1.60 per gram, with the relatively small amount of Pd doping resulting in only a modest increase in overall cost. This cost is comparable to non-precious metal materials such as NLTO and LSTNC, which are priced at $0.30 and $0.36 per gram, respectively. In contrast, the Ru-doped R-PSCFRu material, requiring a significantly higher doping level, incurs a much higher cost of approximately $3.43 per gram. These findings highlight that while Pd doping slightly increases the cost, PBFPd$_{0.1}$ offers an optimal balance between high performance and cost-effectiveness, especially when compared to other anode materials that rely on larger quantities of precious metals.

Stability and structural integrity are crucial characteristics sought in potential anode materials for practical SOFC applications [41,46]. In this context, Fig. 6 provides insights into the stability and structural

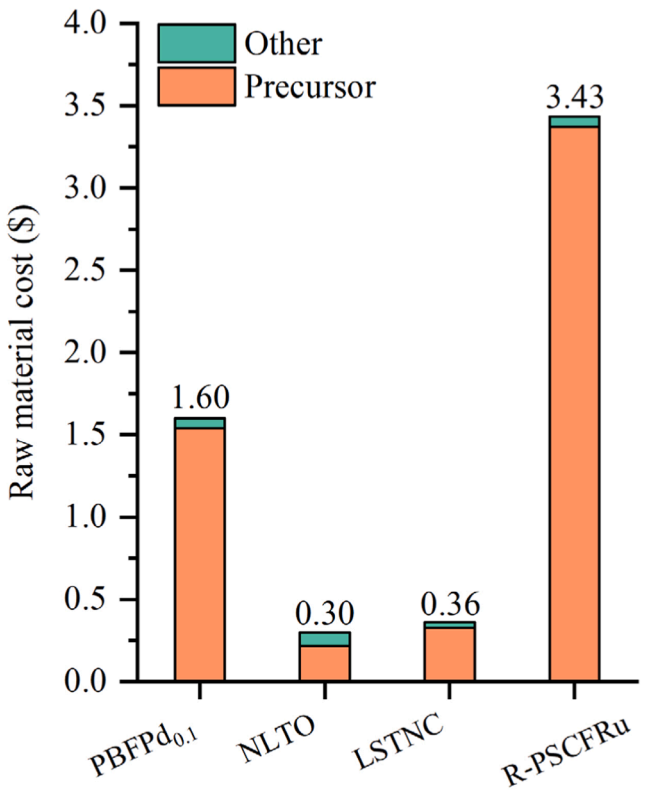

Fig. 5. Cost comparison of $PBFPd_{0.1}$ with other materials. Precursor components and their corresponding costs are detailed in Table SX, with additional materials primarily including EDTA, CA, and ammonia.

characterization of cells utilizing the optimal $PBFPd_{0.1}$-SDC anode materials under various atmospheric conditions. Fig. 6a demonstrates the robust stability of the cell equipped with a $PBFPd_{0.1}$-SDC anode in an H_2 atmosphere (80 sccm) at 700 °C for 150 h. The cell maintains a steady voltage of approximately 0.7 V under a constant current density of 215 mA cm^2, showcasing strong durability and effective performance in a reducing atmosphere. Additionally, Fig. 6b investigates the cell voltage stability in a wet C_2H_6 atmosphere (80 sccm) at 700 °C to assess the robustness of the anode in a hydrocarbon-rich environment. The voltage remains stable at approximately 0.55 V with a current density of 178 mA cm^2 throughout a 90-h discharge period, indicating that the anode can efficiently catalyze hydrocarbon fuels with good stability. In contrast, the cell equipped with a PBF-SDC anode displays significantly poorer discharge performance, achieving only a current density of 72 mA cm^2 for around 50 h as depicted in **Fig. S11**. Additionally, the $PBFPd_{0.2}$-SDC anode demonstrates a relatively lower discharge voltage and a shorter discharge duration at the same current density of 178 mA cm^{-2} compared to the $PBFPd_{0.1}$-SDC anode. It is worth noting that, although $PBFPd_{0.1}$ shows the best discharge performance, all three cells exhibit degradation after long-term discharges of varying durations. To explore the role of Pd doping in enhancing coking resistance and understanding the degradation mechanisms of the cells under C_2H_6 conditions, we employed SEM, XRD and Raman tests. After long-term stability testing, under the continuous effect of high temperature, the particle size of Pd nanoparticles exhibited a coarsening phenomenon (**Fig. S12**). Especially after the ethane test, this phenomenon occurred because of carbon deposition, which promoted the agglomeration and coarsening between the particles [47,48]. Fig. 6c displays the XRD patterns of the $PBFPd_{0.1}$-SDC anode before and after testing in a C_2H_6 atmosphere. The pattern, consisting of $PBFPd_{0.1}$ and SDC phases, remains unchanged following the test, further indicating strong coke resistance under C_2H_6 conditions. In contrast, the XRD pattern of $PBFPd_{0.2}$ shows phase decomposition, with additional Fe and BaO phases observed, which could be attributed to the performance degradation (**Fig. S13b**). Meanwhile, although the phase of PBF remains stable after C_2H_6 testing, its catalytic performance is relatively poor due to the absence of Pd doping (**Fig. S13a**). The Raman spectra of the three anodes before and after testing in a C_2H_6 atmosphere are compared in Fig. 6d and **Fig. S14**. The spectra displays prominent D and G bands, characteristic of carbon species, with increased intensity after testing that indicates carbon deposition on the anode surfaces, a common occurrence with hydrocarbon fuels [44,45]. Notably, both the PBF-SDC anode and $PBFPd_{0.2}$-SDC anodes show considerable carbon deposition post-test,

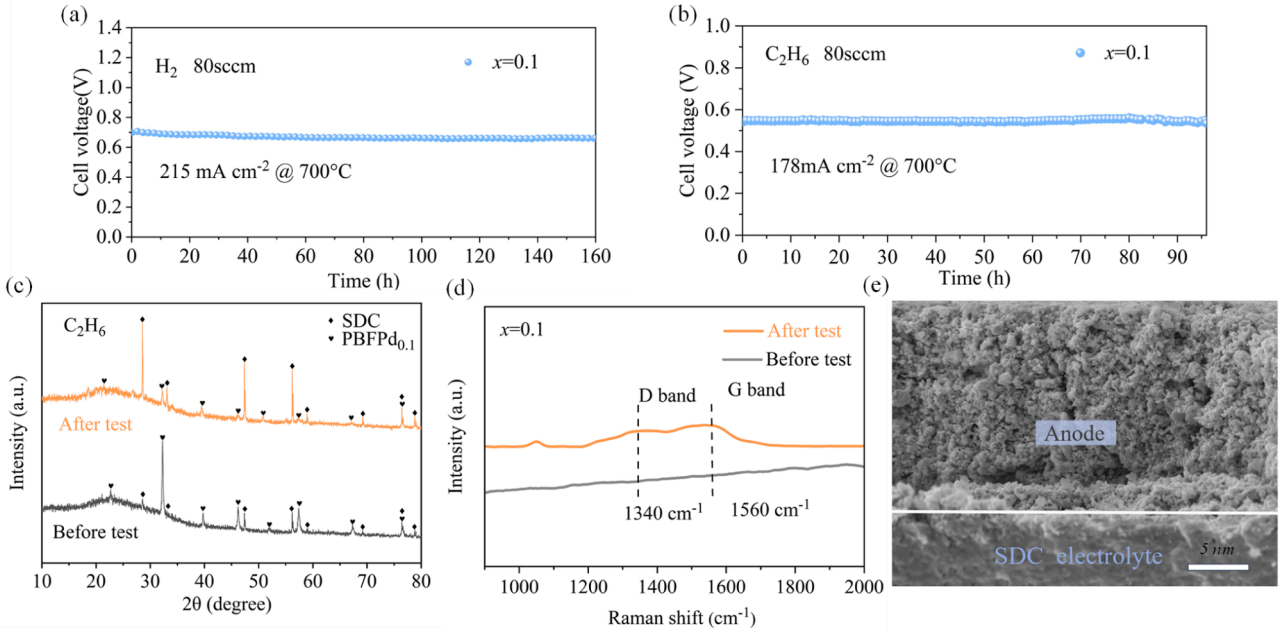

Fig. 6. Stability and structural characterization of $PBFPd_{0.1}$ anode: (a) Stability test in H_2 (80 sccm) at 700 °C under a constant current density of 215 mA cm^{-2}; (b) Stability test in C_2H_6 (80 sccm) at 700 °C under a constant current density of 178 mA cm^{-2}; (c) XRD patterns of PBFPdx-SDC before and after the test in C_2H_6; (d) Raman spectra of PBFPdx-SDC before and after the test in C_2H_6; (e) Cross-section of the $PBFPd_{0.1}$-SDC after the test in C_2H_6.

with carbon peak intensities significantly higher than that of the $PBFPd_{0.1}$-SDC anode. For the PBF-SDC anode, the absence of Pd doping results in poor catalytic performance, preventing the re-vaporization of deposited carbon, thereby causing performance degradation. Similarly, the $PBFPd_{0.2}$-SDC anode experiences decreased catalytic performance due to phase decomposition, along with substantial coke accumulated. In summary, the $PBFPd_{0.1}$-SDC catalyst exhibits superior catalytic performance and stability due to the excellent anti-coking properties and catalytic activity of the Pd nanoparticles, along with a stable phase structure. However, since Pd does not fully cover the perovskite main phase, some coking still occurs.

4. Conclusion

This study demonstrates that palladium-doped $PrBaFe_2O_{5+\delta}$ (PBF) anodes exhibit significantly enhanced electrochemical performance and chemical stability compared to pristine PBF, particularly when operating on hydrogen and ethane fuels under low-humidity conditions. The $PBFPd_{0.1}$ anode, with its superior oxidation properties and stability, delivers optimal performance, establishing Pd-doped PBF as a highly promising nickel-free anode material for SOFCs. This approach addresses key challenges associated with traditional nickel-based anodes, such as coking and high steam-to-carbon requirements, and facilitates the design of more efficient, low-emission SOFC systems. While the high cost and rarity of palladium present scalability challenges, these may be mitigated by reducing Pd doping levels or exploring more economical alternatives. Additionally, Since the nanoparticles do not fully cover the perovskite main phase, allowing coking to still occur, increasing the coverage density of anti-coking nanoparticles remains an important focus for further research. Overall, the substantial performance gains and mechanistic insights provided by this study underscore Pd doping as a promising strategy for advanced SOFC anodes, contributing to cleaner and more efficient energy solutions.

CRediT authorship contribution statement

Shuo Zhai: Writing – review & editing, Formal analysis, Data curation, Conceptualization. **Junyu Cai:** Writing – original draft, Formal analysis, Data curation. **Idris Temitope Bello:** Writing – review & editing. **Xi Chen:** Formal analysis. **Na Yu:** Investigation. **Rubao Zhao:** Validation, Formal analysis. **Xingke Cai:** Resources. **Yunhong Jiang:** Investigation. **Meng Ni:** Writing – review & editing, Supervision, Conceptualization. **Heping Xie:** Supervision, Resources, Conceptualization.

Declaration of competing interest

The authors declare that they have no known competing financial interests or personal relationships that could have appeared to influence the work reported in this paper.

Acknowledgments

This work was supported by National Natural Science Foundation of China Project (Grant No. 52402290). We are grateful for the Guangdong Basic and Applied Basic Research Committee Foundation (Grant No. 2023A1515110316, 2024A1515011848), Project of Strategic Importance Program of The Hong Kong Polytechnic University (P0035168), Shenzhen Science and Technology Program (No. JCYJ20241202300277) and the Centre for Advances in Reliability and Safety (CAiRS), Hong Kong SAR, China, admitted under AIR@InnoHK Research Cluster. The authors also acknowledge the assistance on HRTEM observation received from the Electron Microscope Center of Shenzhen University.

Supplementary materials

Supplementary material associated with this article can be found, in the online version, at doi:10.1016/j.adapen.2025.100206.

Data availability

Data will be made available on request.

References

[1] Zhai S, Xie H, Cui P, Guan D, Wang J, Zhao S, et al. A combined ionic Lewis acid descriptor and machine-learning approach to prediction of efficient oxygen reduction electrodes for ceramic fuel cells [J]. Nat Energy 2022;7:866–75.
[2] Duan C, Kee R, Zhu H, Sullivan N, Zhu L, Bian L, et al. Highly efficient reversible protonic ceramic electrochemical cells for power generation and fuel production [J]. Nat Energy 2019;4:230–40.
[3] Ni M, Shao Z. Fuel cells that operate at 300 to 500 C [J]. Science (1979) 2020;369:138–9.
[4] Xu Q, Guo Z, Xia L, He Q, Li Z, Temitope I, et al. A comprehensive review of solid oxide fuel cells operating on various promising alternative fuels [J]. Energy Convers Manag 2022;253:115175.
[5] Carrette L, Friedrich K, Stimming U. Fuel cells-fundamentals and applications. Fuel Cells; 2001.
[6] Hibino T, Hashimoto A, Inoue T, Tokuno JI, Yoshida SI, Sano M. A low-operating-temperature solid oxide fuel cell in hydrocarbon-air mixtures [J]. Science (1979) 2000;288:2031–3.
[7] Duan C, Kee RJ, Zhu H, Karakaya C, Chen Y, Ricote S, et al. Highly durable, coking and sulfur tolerant, fuel-flexible protonic ceramic fuel cells [J]. Nature 2018;557:217–22.
[8] Shao Z, Haile SM. A high-performance cathode for the next generation of solid-oxide fuel cells [J]. Nature 2004;431:170–3.
[9] Zhai S, Xie H, Chen B, Ni M. A rational design of FeNi alloy nanoparticles and carbonate-decorated perovskite as a highly active and coke-resistant anode for solid oxide fuel cells [J]. Chem Eng J 2022;430:132615.
[10] Thommy L, Benamira M, Jardiel T, Günes V, Joubert O, Caldes M. Ru exsolution in substituted $La_{0.75}Sr_{0.25}Cr_{0.5}Mn_{0.5}O_{3-\delta}$ compound as anode material for an IT-SOFCs [J]. Mater Chem Phys 2021;268:124724.
[11] Chen K, He S, Li N, Cheng Y, Ai N, Chen M, et al. Nb and Pd co-doped $La_{0.57}Sr_{0.38}Co_{0.19}Fe_{0.665}Nb_{0.095}Pd_{0.05}O_{3-\delta}$ as a stable, high performance electrode for barrier-layer-free Y_2O_3-ZrO_2 electrolyte of solid oxide fuel cells [J]. J Power Sources 2018;378:433–42.
[12] Shin TH, Okamoto Y, Ida S, Ishihara T. Self-recovery of Pd nanoparticles that were dispersed over La(Sr)Fe(Mn)O_3 for intelligent oxide anodes of solid-oxide fuel cells [J]. Chem Eur J 2012;18:11695–702.
[13] Liu C, Wang F, Ni Y, Wang S, Qian B, Ni Q, et al. Ta-doped $PrBaFe_2O_{5+\delta}$ double perovskite as a high-performance electrode material for symmetrical solid oxide fuel cells [J]. Int J Hydrogen Energy 2023;48:9812–22.
[14] Lee D, Kim D, Son SJ, Y-i K, Lee Y, Ahn J-H, et al. Simultaneous A-and B-site substituted double perovskite ($AA'B_2O_{5+\delta}$) as a new high-performance and redox-stable anode material for solid oxide fuel cells [J]. J Power Sources 2019;434:226743.
[15] Li X, Li R, Tian Y, Gao Y, Zhu S, Jin F, et al. Tuning $Pr_{0.5}Ba_{0.5}FeO_{3-\delta}$ cathode to enhanced stability and activity via Ca-doping for symmetrical solid oxide fuel cells [J]. Int J Hydrogen Energy 2024;60:650–6.
[16] Bello IT, Guan D, Yu N, Li Z, Song Y, Chen X, et al. Revolutionizing material design for protonic ceramic fuel cells: bridging the limitations of conventional experimental screening and machine learning methods [J]. Chem Eng J 2023;477:147098.
[17] Marcucci A, Zurlo F, Sora IN, Luisetto I, Licoccia S, Di BE. Pd-doped lanthanum ferrites for symmetric solid oxide fuel cells (SSOFCs) [J]. Materialia (Oxf) 2019;8:100460.
[18] Kresse G, Furthmüller J. Efficiency of ab-initio total energy calculations for metals and semiconductors using a plane-wave basis set [J]. Comput Mater Sci 1996;6:15–50.
[19] Kresse G, Joubert D. From ultrasoft pseudopotentials to the projector augmented-wave method [J]. Phys Rev B 1999;59:1758.
[20] Blöchl PE. Projector augmented-wave method [J]. Phys Rev B 1994;50:17953.
[21] Perdew JP, Burke K, Ernzerhof M. Generalized gradient approximation made simple [J]. Phys Rev Lett 1996;77:3865.
[22] Pack JD, Monkhorst HJ. Special points for Brillouin-zone integrations"—a reply [J]. Phys Rev B 1977;16:1748.
[23] Wang V, Xu N, Liu J-C, Tang G, Geng W-T. VASPKIT: a user-friendly interface facilitating high-throughput computing and analysis using VASP code [J]. Comput Phys Commun 2021;267:108033.
[24] Shannon RD. Revised effective ionic radii and systematic studies of interatomic distances in halides and chalcogenides [J]. Acta Crystallogr Sect A 1976;32:751–67. : crystal physics, diffraction, theoretical and general crystallography.
[25] Slater JC. Atomic radii in crystals [J]. J Chem Phys 1964;41:3199–204.
[26] Bello IT, Yu N, Zhai S, Song Y, Zhao S, Cheng C, et al. Effect of engineered lattice contraction and expansion on the performance and CO_2 tolerance of $Ba_{0.5}Sr_{0.5}Co_{0.7}Fe_{0.3}O_{3-\delta}$ functional material for intermediate temperature solid oxide fuel cells [J]. Ceram Int 2022;48:21416–27.

[27] Kim JH, Jang K, Lim D-K, Ahn S, Oh D, Kim H, et al. Self-assembled nano-composite perovskites as highly efficient and robust hybrid cathodes for solid oxide fuel cells [J]. J Mater Chem A 2022;10:2496–508.
[28] Park J, Zou J, Yoon H, Kim G, Chung JS. Electrochemical behavior of $Ba_{0.5}Sr_{0.5}Co_{0.2-x}Zn_xFe_{0.8}O_{3-\delta}$ (x= 0–0.2) perovskite oxides for the cathode of solid oxide fuel cells [J]. Int J Hydrogen Energy 2011;36:6184–93.
[29] Ren R, Wang Z, Meng X, Xu C, Qiao J, Sun W, et al. Boosting the electrochemical performance of Fe-based layered double perovskite cathodes by Zn^{2+} doping for solid oxide fuel cells [J]. ACS Appl Mater Interfaces 2020;12:23959–67.
[30] Lim C, Yang Y, Sin Y-w, Choi S, Kim G. Ca-and Ni-doped $Pr_{0.5}Ba_{0.5}FeO_{3-\delta}$ as a highly active and robust cathode for high-temperature solid oxide fuel cell [J]. Energy Fuels 2020;34:11458–63.
[31] Song Y, Li H, Xu M, Yang G, Wang W, Ran R, et al. Infiltrated NiCo alloy nanoparticle decorated perovskite oxide: a highly active, stable, and antisintering anode for direct-ammonia solid oxide fuel cells [J]. Small 2020;16:2001859.
[32] Marcucci A, Zurlo F, Sora IN, Placidi E, Casciardi S, Licoccia S, et al. A redox stable Pd-doped perovskite for SOFC applications [J]. J Mater Chem A 2019;7:5344–52.
[33] Baek S-S, Park K-Y, Lee T-H, Lee N, Seo Y, Song S-J, et al. PdO-doped $BaZr_{0.8}Y_{0.2}O_{3-\delta}$ electrolyte for intermediate-temperature protonic ceramic fuel cells [J]. Acta Mater 2014;66:273–83.
[34] Bello IT, Yu N, Song Y, Wang J, Chan TS, Zhao S, et al. Electrokinetic insights into the triple ionic and electronic conductivity of a novel nanocomposite functional material for protonic ceramic fuel cells [J]. Small 2022;18:2203207.
[35] Guan D, Ryu G, Hu Z, Zhou J, Dong C-L, Huang Y-C, et al. Utilizing ion leaching effects for achieving high oxygen-evolving performance on hybrid nanocomposite with self-optimized behaviors [J]. Nat Commun 2020;11:3376.
[36] Zhai S, Zhao R, Liao H, Fu L, Hao S, Cai J, et al. Enhancing layered perovskite ferrites with ultra-high-density nanoparticles via cobalt doping for ceramic fuel cell anode [J]. J Energy Chem 2024;96:39–48.
[37] Kothari M, Jeon Y, Miller DN, Pascui AE, Kilmartin J, Wails D, et al. Platinum incorporation into titanate perovskites to deliver emergent active and stable platinum nanoparticles [J]. Nat Chem 2021;13:677–82.
[38] Song S, Zhou J, Su X, Wang Y, Li J, Zhang L, et al. Operando X-ray spectroscopic tracking of self-reconstruction for anchored nanoparticles as high-performance electrocatalysts towards oxygen evolution [J]. Energy Environ Sci 2018;11:2945–53.
[39] Fabbri E, Nachtegaal M, Binninger T, Cheng X, Kim B-J, Durst J, et al. Dynamic surface self-reconstruction is the key of highly active perovskite nano-electrocatalysts for water splitting [J]. Nat Mater 2017;16:925–31.
[40] Ciucci F, Chen C. Analysis of electrochemical impedance spectroscopy data using the distribution of relaxation times: a Bayesian and hierarchical Bayesian approach [J]. Electrochim Acta 2015;167:439–54.
[41] Bello IT, Zhai S, He Q, Cheng C, Dai Y, Chen B, et al. Materials development and prospective for protonic ceramic fuel cells [J]. Int J Energy Res 2022;46:2212–40.
[42] Su C, Wu Y, Wang W, Zheng Y, Ran R, Shao Z. Assessment of nickel cermets and $La_{0.8}Sr_{0.2}Sc_{0.2}Mn_{0.8}O_3$ as solid-oxide fuel cell anodes operating on carbon monoxide fuel [J]. J Power Sources 2010;195:1333–43.
[43] Oh J, Joo S, Lim C, Kim HJ, Ciucci F, Wang JQ, et al. Precise modulation of triple-phase boundaries towards a highly functional exsolved catalyst for dry reforming of methane under a dilution-free system [J]. Angew Chem Int Edit 2022;61:e202204990.
[44] Bello IT, Song Y, Yu N, Li Z, Zhao S, Maradesa A, et al. Evaluation of the electrocatalytic performance of a novel nanocomposite cathode material for ceramic fuel cells [J]. J Power Sources 2023;560:232722.
[45] Xiong X, Yu J, Huang X, Zou D, Song Y, Xu M, et al. Slightly ruthenium doping enables better alloy nanoparticle exsolution of perovskite anode for high-performance direct-ammonia solid oxide fuel cells [J]. J Mater Sci Technol 2022;125:51–8.
[46] Bello IT, Zhai S, He Q, Xu Q, Ni M. Scientometric review of advancements in the development of high-performance cathode for low and intermediate temperature solid oxide fuel cells: three decades in retrospect [J]. Int J Hydrogen Energy 2021;46:26518–36.
[47] Weng G, Ouyang K, Lin X, Wen S, Zhou Y, Lei S, et al. Enhanced hydrogen permeability of mixed protonic–electronic conducting membranes through an in-situ exsolution strategy [J]. Adv Funct Mater 2022;32:2205255.
[48] Jo S, Sharma B, Park D-H, J-h M. Materials and nano-structural processes for use in solid oxide fuel cells: a review [J]. J Korean Ceram Soc 2020;57:135–51.